

Minimising the Number of Ranging Sensors verifying Target Positioning Uncertainty

Abstract

Indoor positioning applications are increasingly popular due to the availability of effective and low cost ranging sensors. Many solutions have been proposed recently using these type of sensors to estimate the coordinates (position) of a target within a given target uncertainty. In this paper, we consider the problem of deploying a large scale infrastructure that solves the positioning task with guaranteed estimation uncertainty while minimising the number of ranging sensors. To this end, we adopt a two steps procedure. In the first step, we identify a basic cell structure compounded of a small number of sensors deployed in symmetric configurations. We study the problem in general terms and we specifically focus on how to maximise the area covered by this basic structure using the smallest possible number of three ranging sensors. In the second step, we use this basic cell as an elementary tile structure to be used in standard coverage algorithm minimising the portion of space left uncovered. The approach is validated through a large number of simulations and experimental results.

Keywords: Optimal sensor placement, Ranging-based positioning, uncertainty analysis

1. Introduction

2 Given an entity (e.g., a person, a robot or a valuable asset of any kind)
3 and given an environment, the positioning problem is about the use of some
4 external measurements to find its cartesian coordinates at a given time,
5 whereas the localisation problem is about using external measurements and
6 ego-motion information to reconstruct its pose (cartesian coordinates + ori-
7 entation) and to track it over time [1]. Both problems are instrumental to
8 a large class of important industrial applications, and their solution is par-
9 ticularly difficult in the environments where the satellite-based positioning
10 systems are not available or reliable.

11 The increasing availability of low cost accurate sensors has democratised
12 the positioning and localisation technology disclosing important opportuni-
13 ties for its penetration in large indoor environments, once believed the most
14 impervious to its application. An important example of this innovative type
15 of sensors are the Ultra-Wide-Band (UWB) communication modules. An
16 UWB node can generate a very narrow impulse that is robust to multipath
17 fading and interference. Therefore, it is possible to set up a measurement
18 system based on time-of-arrival (ToA) information and producing ranging
19 measurement with an accuracy of a few centimetres. Even if this new type
20 of sensors have made accurate positioning affordable, they require to set up
21 an maintain an important infrastructure. This leads us to the sensor place-
22 ment problem: finding a deployment that guarantees an assigned maximum
23 target uncertainty and that requires the least number of sensors. As we will
24 discuss in the paper, the problem is known to be NP-Hard, and in order for
25 a solution to scale to environments of realistic size, it has to be necessarily
26 sub-optimal. With these considerations in mind, the relevance of a solution
27 for optimal sensor placement has to be evaluated on its ability to meet a
28 number of practical requirements such as: **R1.** producing solutions for large
29 environments in an acceptable time (scalability), **R2.** working with environ-
30 ments of arbitrary shape (generality), **R3.** keeping the number of deployed
31 sensors close to the minimal and anyway very small (efficiency), **R4.** guaran-
32 teeing specified levels of uncertainty by countering all possible effects (e.g., of
33 geometric nature) that could amplify the positioning error (reliability), **R5.**
34 it has to consider physical limitations of the sensors (sensor limitations). As
35 regards, the last requirement, we should observe that the ranging uncertainty
36 is a function of the distance between the source and the emitter. For exam-
37 ple, light based (e.g., LiDAR) or acoustic (e.g., Sonars) ranging systems are
38 naturally limited by the maximum sensing distance [2]. Typical RF ranging
39 systems suffer the same limitations. This has been observed for RSSI sig-
40 nals [3] but also for the ToA based measurements of UWB nodes, both in
41 Line of Sight (LoS) [4] and in non-LoS [5] conditions.

42 **Related Work.** The sensor placement problem has been widely investi-
43 gated in the past for different types of sensors. For example, [6] proposed a
44 visual landmark placement algorithm in order to meet a desired target un-
45 certainty. This solution considers the existence of a fixed pattern, equilateral
46 triangles with landmarks on the vertices, that has been shown to be optimal
47 to reach the minimum uncertainty [7].

48 Redondi et al. [8] presented Tabu Search heuristic algorithm for finding

49 the optimal deployment pattern of sensor nodes for an indoor localisation
50 system based on Received Signal Strength (RSS). The approach considers a
51 fixed number of sensors and uses the Cramer Rao Lower Bound (CRLB) as
52 the optimality index to minimise the overall localisation error. In the same
53 line, other papers [9, 10] address the range sensors placement problems, with
54 the mean-square localisation error being used as the optimisation index. The
55 proposed solutions provide near-optimal deployment patterns on a free plane
56 without considering the physical constraints of the environment. Besides, the
57 authors do not offer any clue on the actual computational costs of the opti-
58 misation algorithm. With respect to these papers, our problem is somewhat
59 dual: rather than minimising the uncertainty given the number of nodes, we
60 look for the minimal number of nodes guaranteeing a target uncertainty and
61 then build the deployment on it.

62 Chepuri et al. [11] proposes a solution for selecting the optimal deploy-
63 ment pattern of UWB nodes. The problem is modelled as the the design of
64 a sparse selection vector and its solution is based on the random selection
65 of a sub-set of sensors which are randomly located on a well-shaped grid
66 structure. Hence, its application cannot be generalised to environments of
67 generic shape.

68 Information-theoretic-based approaches [12, 13] are popular methods for
69 optimal sensor placements, suitable for selection of heterogeneous sensors
70 used for both observation and actuations. In [14], a sensor selection strategy
71 for target localisation based on the maximum likelihood estimator is pre-
72 sented. The algorithm chooses the sensor observation that reduces the most
73 the entropy on the target location, taking into account the prior target po-
74 sition pdf. The selection procedure is performed iteratively using a heuristic
75 algorithm selecting one sensor per step. [15] investigates a unique scalar
76 measure for the spread of the uncertainty in the structural parameter values
77 using the Fisher information matrix. By developing a relationship between
78 measurement redundancy and information entropy, the optimal set of sensor
79 configurations that minimises the entropy measure is obtained. The approach
80 has a strong relationship with the determinant of the inverse of Fisher infor-
81 mation matrix, which encompasses the information about the values of the
82 structural model parameters based on the data from all measured positions.
83 Another approach based on [15] takes the knowledge of the prior distribution
84 into account within a Bayesian framework for the placement of multi-type
85 sensors (measurement and system actuation) of a dynamical system [16].
86 Here a heuristic sequential method was used for selecting the optimal loca-

87 tions of different types of sensors based on the overall Information Entropy.
88 The downside of the aforementioned entropy-based methodologies is a very
89 high computational cost to solve the discrete optimisation and obtain good
90 estimates of sensor configurations that correspond to information entropy
91 values close to the minimum information entropy.

92 The idea of seeking the optimal deployment of range sensors within fixed
93 patterns is explored by several authors. In a number of different proposals [6,
94 17, 18, 19], the approach is to first fix a grid of “candidate” positions for
95 the sensors, and then apply non-convex optimisation to find the optimal
96 deployment of sensors limiting the search to the grid. As observed by Chepuri
97 et al. [17], the performance of an algorithm of this kind is strongly related
98 to the choice of the search grid. A coarse grained grid may prevent the
99 algorithm from a deployment guaranteeing the required target uncertainty,
100 while a small grid size may easily make the problem intractable.

101 As a final and additional important point, none of the papers cited above
102 dealing with ranging sensors considers the point that we have generally de-
103 fined as sensor limitations (i.e., the limited sensing range). We would like
104 also to remark that, in spite of the rich literature on the topic and of the
105 constant reduction of the hardware costs over the past years, the sensor de-
106 ployment problem remains a very active research area. Much of the scientific
107 interest lies in the difficulty of achieving scalable solutions, of deploying an-
108 chors to difficult-to reach locations, of keeping in check the maintenance cost
109 of the system, and of managing the communication protocol between the
110 anchors and with the target.

111 **Paper Contribution.** In this paper, we propose a sensor placement solution
112 respecting the five requirements stated above. Our solution builds on a key
113 observation from Chen et al. [20]: an optimal ranging sensor deployment
114 follows exact symmetrical patterns. For example, the optimal pattern for
115 the three sensors case is an equilateral triangle, for four is a square, for six is
116 given by two nested equilateral triangles (one triangle inside the other), etc.
117 This observation leads us to search for the optimal symmetric configuration
118 of a set of n ranging sensors (henceforth referred to as *anchors*) that covers
119 a region \mathcal{P}_n respecting some constraints. The constraints are for us of two
120 types: 1. each point in the region must fall within the sensing range (which
121 is set to a finite and known value r) of an adequate number of anchors, 2.
122 the positioning uncertainty within this area should be less than the desired
123 target uncertainty. Notice that by “optimal” we mean the configuration
124 that respects the constraints with the minimal number of anchors. Once

125 this region has been identified and characterised, it can be used as a basic
 126 “tile” in a geometric covering algorithm [21]. Our first contribution is a
 127 characterisation of the geometric properties of the region \mathcal{P}_n and an algorithm
 128 that solves the optimisation problem.

129 The minimal number of anchors that solve the problem is $n = 3$. How-
 130 ever, we show as our second, and probably most important, contribution
 131 that the minimal “tile” that we should consider is not necessarily \mathcal{P}_3 , but it
 132 is possible to find a region \mathcal{P}_2 with larger coverage and with the same posi-
 133 tioning uncertainty. The validity of the approach is shown by a large number
 134 of simulations and experimental evidence.

135 The paper is organised as follows. In Section 2, we offer a quick overview
 136 of the main previous results and ideas the paper builds on. In Section 3,
 137 we provide a geometric characterisation of the region \mathcal{P}_n and we describe an
 138 algorithm to optimise the anchor configuration to cover \mathcal{P}_n with guaranteed
 139 positioning performance and minimising the number of anchors. In Section 4,
 140 we focus our attention on the case of the cell covered with the minimum
 141 possible number of anchors ($n = 3$). In particular, we show that, for every
 142 \mathcal{P}_3 configuration, we can find an equivalent \mathcal{P}_2 with the same maximum
 143 uncertainty and with a larger coverage. The approach is validated through
 144 simulation data in Section 5 and through experiments in Section 6. Finally,
 145 in Section 7, we state our conclusions and announce future work directions.

146 2. Background Material

147 We consider the problem of estimating the position of a target within an
 148 indoor environment. To this end, we will use ranging sensors that, in the
 149 ideal case, produce a measurement modelled by the measurement function:

$$\ell_i = h_i(\mathbf{p}) = \sqrt{(X_i - x)^2 + (Y_i - y)^2}, \quad (1)$$

150 with $\mathbf{a}_i = [X_i, Y_i]^T$ being the Cartesian coordinates of the i -th anchor and
 151 with $\mathbf{p} = [x, y]^T \in \mathcal{P}$ being the coordinates of the target position to be
 152 estimated. The results presented below are totally agnostic both to the
 153 choice of the sensor module (e.g., based on radio frequency, ultrasonic or
 154 light signals) and to the measurement technique (e.g., measuring the radio
 155 signal strength, the echo, the time-stamped values).

156 Estimating the coordinates of a target \mathbf{p} at a given time by using the
 157 ranging measurements is known as a positioning problem, and its solution

158 require at least $n \geq 3$ measurements from non-collinear anchors [22]. On the
 159 contrary, if the target moves with known dynamics a localisation problem
 160 is adopted, whose solution leverages the motion information as well; there-
 161 fore, under minimal assumptions, the minimum number of anchors required
 162 reduces to $n = 2$ [23]. In this paper, we will restrict the focus to the position-
 163 ing problem. We will make the realistic assumptions that measurements are
 164 affected by noise, and therefore the estimated position will be uncertain. We
 165 remark that the uncertainty on the position is amplified when it is used to
 166 reconstruct the pose for dynamic targets [1, 24], thus making the discussion
 167 below relevant also for the localisation problem.

168 Because of the noise, the measurement function (1) takes the more real-
 169 istic form:

$$\bar{\ell}_i = h_i(\mathbf{p}) + \eta_i = \ell_i + \eta_i. \quad (2)$$

170 We will assume that the uncertainties η_i are zero mean and uncorrelated.
 171 Hence, using the expected operator $\mathbb{E}\{\cdot\}$, we have $\mathbb{E}\{\eta_i\eta_j\} = 0$ if $i \neq j$
 172 and $\mathbb{E}\{\eta_i^2\} = \sigma_i^2$, which can be expressed more compactly with the vectorial
 173 form $\boldsymbol{\eta} = [\eta_1, \dots, \eta_n]^T$, i.e., $\boldsymbol{\Sigma}_\eta = \mathbb{E}\{\boldsymbol{\eta}\boldsymbol{\eta}^T\} = \text{diag}(\sigma_1^2, \dots, \sigma_n^2)$. Since (1)
 174 is nonlinear, the problem of finding a suitable estimate $\hat{\mathbf{p}}$ of \mathbf{p} can be effec-
 175 tively solved using the following Nonlinear Weighted Least Squares (NWLS)
 176 problem

$$\hat{\mathbf{p}} = \arg \min_{\mathbf{p}} \sum_{i=1}^n \frac{(\bar{\ell}_i - h_i(\mathbf{p}))^2}{\sigma_i^2}. \quad (3)$$

177 An effective solution is given by the iterative Gauss-Newton solution, which,
 178 solves a point-wise linearised WLS problem

$$\bar{\boldsymbol{\ell}} \approx H_k \hat{\mathbf{p}}_{k+1} + \boldsymbol{\eta} \Rightarrow \hat{\mathbf{p}}_{k+1} = (H_k^T \boldsymbol{\Sigma}_\eta^{-1} H_k)^{-1} H_k^T \boldsymbol{\Sigma}_\eta^{-1} \bar{\boldsymbol{\ell}} = H_k^\dagger \bar{\boldsymbol{\ell}}, \quad (4)$$

179 where $\bar{\boldsymbol{\ell}} = [\bar{\ell}_1, \dots, \bar{\ell}_n]^T$ is the vector of measurements (2),

$$H_k = \frac{\partial h}{\partial \hat{\mathbf{p}}_k} \begin{bmatrix} \lambda_{x_1}(\hat{\mathbf{p}}_k) & \lambda_{y_1}(\hat{\mathbf{p}}_k) \\ \lambda_{x_2}(\hat{\mathbf{p}}_k) & \lambda_{y_2}(\hat{\mathbf{p}}_k) \\ \vdots & \vdots \\ \lambda_{x_n}(\hat{\mathbf{p}}_k) & \lambda_{y_n}(\hat{\mathbf{p}}_k) \end{bmatrix}, \quad (5)$$

180 is the Jacobian of the measurement vector $h(\mathbf{p})$, $\lambda_{x_i}(\hat{\mathbf{p}}_k) = \frac{\hat{x}_k - X_i}{\hat{\ell}_{i,k}}$, $\lambda_{y_i}(\hat{\mathbf{p}}_k) =$
 181 $\frac{\hat{y}_k - Y_i}{\hat{\ell}_{i,k}}$, and $\hat{\ell}_{i,k} = \sqrt{(\hat{x}_k - X_i)^2 + (\hat{y}_k - Y_i)^2}$. In this expression, $\hat{\mathbf{p}}_k$ is the es-
 182 timate of \mathbf{p} at the k -th iteration of the NWLS, and is used to derive the

183 updated estimates $\hat{\mathbf{p}}_{k+1}$. The standard approach mandates to iterate the
 184 gradient descent steps up until $\|\hat{\mathbf{p}}_{k+1} - \hat{\mathbf{p}}_k\| \leq e_{\mathbf{p}}$, where $e_{\mathbf{p}}$ is a user defined
 185 accuracy threshold. However, by exploiting geometric properties, it is
 186 possible to find an alternative technique, known as the G-WLS [25], which
 187 requires only two WLS iterations to reach the optimal theoretical bound in
 188 standard operative conditions. The first step is the solution of a linearised
 189 multilateration problem using a standard WLS, while the second step corrects
 190 the result by injecting the information on anchor geometry captured by
 191 the Geometric Dilution of Precision (GDoP) for positioning problems [26].
 192 The two-steps algorithm leads to a position estimation error $\tilde{\mathbf{p}} = \mathbf{p} - \hat{\mathbf{p}}$ with
 193 an uncertainty given by

$$\bar{\Sigma}_{\tilde{\mathbf{p}}_k} = (H_k^T \mathbb{E} \{ \bar{\ell} \ell^T \}^{-1} H_k)^{-1} = (H_k^T \Sigma_{\boldsymbol{\eta}}^{-1} H_k)^{-1}.$$

194 As reported in [25], in the case of zero-mean and Gaussian uncertainties
 195 $\boldsymbol{\eta} = [\eta_1, \dots, \eta_m]^T$, the solution of the two-step G-WLS almost surely reaches
 196 the CRLB [27]

$$C(\mathbf{p}) = (H^T \Sigma_{\boldsymbol{\eta}}^{-1} H)^{-1}, \quad (6)$$

197 where H is the value of (5) evaluated in the actual position \mathbf{p} . The CRLB is
 198 a measure of the minimum theoretical estimation uncertainties achievable by
 199 an estimator, hence this certifies the effectiveness of the two steps approach.

200 Moreover, in the assumption of homoscedasticity of the ranging uncer-
 201 tainties, i.e., $\Sigma_{\boldsymbol{\eta}} = \sigma_{\ell}^T I_m$, we have

$$\bar{\Sigma}_{\tilde{\mathbf{p}}_k} = \sigma_{\ell}^2 (H_k^T H_k)^{-1}. \quad (7)$$

202 This quantity is tightly related to the GDoP $g(\mathbf{p})$ [28, 29]:

$$g(\mathbf{p}) = \sqrt{\text{Tr}((H_k^T H_k)^{-1})} = \frac{\sqrt{\text{Tr}(\bar{\Sigma}_{\tilde{\mathbf{p}}_k})}}{\sigma_{\ell}}, \quad (8)$$

203 where $\text{Tr}(\cdot)$ is the trace of a matrix and $\tilde{\mathbf{p}}_k = \mathbf{p} - \hat{\mathbf{p}}_k$. The lower is the GDoP,
 204 the lower is the uncertainty on $\tilde{\mathbf{p}}_k$, since $(H_k^T H_k)^{-1}$ acts as a multidimensional
 205 gain for the ranging uncertainties.

206 2.1. Problem formulation

207 Since the CRLB (6) can be attained using the G-WLS [25] and it is
 208 intrinsically related to the GDoP (8), we will consider the GDoP as the cost

209 index to guide the optimal deployment of the ranging sensors. In particular,
 210 given the set of all the feasible positions \mathcal{P} , we want to minimise the number n
 211 of ranging anchors deployed in the environment in order to have $g(\mathbf{p}) \leq g^*$,
 212 $\forall \mathbf{p} \in \mathcal{P}$, where g^* is the maximum desired value for the GDoP. We will
 213 explicitly consider *limited sensing range* r for the anchors, which will be
 214 modelled by setting $\bar{\ell}_i = -1$ in (2) if $\ell_i > r$ in (1) (e.g., no echo is detected
 215 in Time-of-Flight ranging sensors).

216 3. Geometric Analysis

217 One common approach to ranging anchors deployment is to first grid the
 218 space \mathcal{P} with a sequence of m points on a grid, displaced at distance d . Next,
 219 by regularly sampling $\mathbf{p}_h \in \mathcal{P}$, $h = 1, \dots, q$, it is possible to compute the
 220 gradients $H_{i,h}$ (the rows of (5)) for the i -th grid position, $i = 1, \dots, m$, in the
 221 h -th sampled position \mathbf{p}_h , $h = 1, \dots, q$. Assuming homoscedasticity for the
 222 uncertainties and using the selection vector $\mathbf{w} = [w_1, w_2, \dots, w_m]^T \in \{0, 1\}^m$,
 223 where $w_i = 1$ if the sensor is placed in the i -th position or zero otherwise, it
 224 is possible to set the following optimisation problem [17]

$$\min_{\mathbf{w} \in \{0,1\}^m} \|\mathbf{w}\|_0 \text{ s.t. } \sigma_\ell^2 \text{Tr} \left(\left(\sum_{i=1}^m w_i H_{i,h}^T H_{i,h} \right)^{-1} \right) \leq \lambda, \forall h \quad (9)$$

225 where the $\|\mathbf{w}\|_0$ is a quasi norm counting the number of non-zero entries of
 226 \mathbf{w} and λ is the desired target uncertainty for the position estimates. Since

$$\text{Tr} \left(\left(\sum_{i=1}^m w_i H_{i,h}^T H_{i,h} \right)^{-1} \right) = \text{Tr} \left((H_h^T H_h)^{-1} \right),$$

227 where H_h is the Jacobian (5) evaluated in position \mathbf{p}_h and for the anchors in
 228 grid position i where $w_i = 1$, the minimisation problem (9) is substantially
 229 equivalent to the GDoP uncertainty gain minimisation in (8) and this further
 230 corroborates our choice of the GDoP as a cost function. With this approach,
 231 the performance very much depends on the grid's choice [17], and it is not
 232 possible to consider a limited sensing range.

233 To overcome these important limitations, we we will consider an approach
 234 in which the search for the optimal configuration is made in a continuous
 235 space. Our idea to reduce the complexity is based on two steps. In the first

236 step, we identify a basic "tile" $\mathcal{P}_n \subseteq \mathcal{P}$, in which n anchors are optimally de-
 237 ployed so that the the GDoP constraint is satisfied, i.e. $g_n(\mathbf{p}) \leq g^*, \forall \mathbf{p} \in \mathcal{P}_n$.
 238 This search is simplified by two facts: 1. the optimal solution can be sought
 239 between the symmetric configurations of the anchors [20], 2. the behaviour
 240 of the GDoP is monotone in the number of anchors $g_n(\mathbf{p}) \geq g_{n+1}(\mathbf{p})$ (i.e.,
 241 given a configuration with n anchors, randomly adding an anchor will never
 242 increase the GDoP). The second fact has an additional benefit: if we consider
 243 two tiles \mathcal{P}_n , any point \mathbf{p} in the overlapping region will respect $g(\mathbf{p}) \leq g^*$.
 244 This leads us to the second step: once the basic tile \mathcal{P}_n structure is defined,
 245 it can be replicated to cover the entire space using standard tile coverage
 246 algorithms (see Section 5.1).

247 3.1. \mathcal{P}_n region

248 In this first part of the discussion, we characterise the most important
 249 properties of the region \mathcal{P}_n . As reported in [20], given a set of $n \geq 3$ anchors
 250 the most convenient configuration for GDoP minimisation is one in which
 251 the anchors are optimally deployed on a circle. Indeed, the matrix H_k in (5)
 252 can be expressed as (the subscript k in (4) is not needed in this context)

$$H = \begin{bmatrix} \cos(\gamma_1) & \sin(\gamma_1) \\ \cos(\gamma_2) & \sin(\gamma_2) \\ \vdots & \vdots \\ \cos(\gamma_n) & \sin(\gamma_n) \end{bmatrix},$$

253 where $\gamma_i = \arctan \frac{y-Y_i}{x-X_i}$, with the evaluation point $\mathbf{p} = [x, y]^T$ and the anchor
 254 position $\mathbf{a}_i = [X_i, Y_i]^T$, which leads to [25]

$$g_n(\mathbf{p}) = \sqrt{\frac{n}{\sum_{i=1}^{n-1} \sum_{j=i+1}^n \sin(\gamma_j - \gamma_i)^2}} = \sqrt{\frac{n}{D_n}}. \quad (10)$$

255 Three important propositions are now stated.

256 **Proposition 1.** *Within the \mathcal{P}_n region, the GDoP $g_n(\mathbf{p})$ is non-increasing*
 257 *with n . As an example, in Figure 1, shows the lower bound $\underline{g} = \min_{\mathbf{p}} g_n(\mathbf{p})$*
 258 *with a dashed line and the upper bound $\bar{g} = \max_{\mathbf{p}} g_n(\mathbf{p})$ with a dotted line.*
 259 *As it is possible to see both decrease with n .*

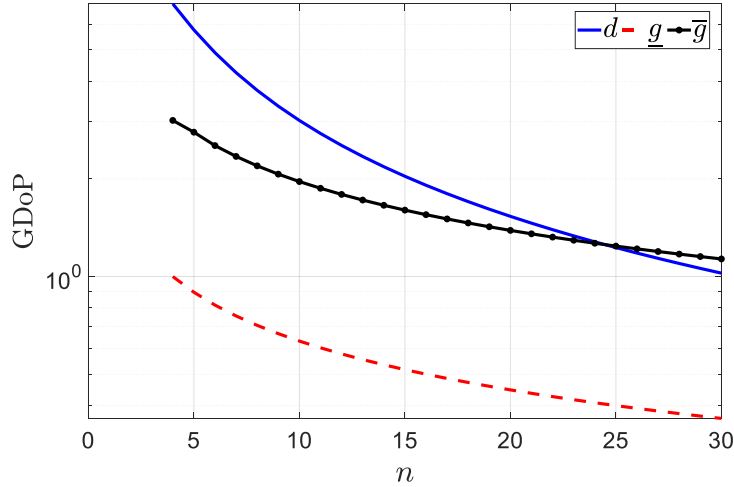


Figure 1: Behaviour of d (solid), \underline{g} (dashed) and \bar{g} as a function of the number of anchors and with a fixed radius δ .

260 **Proposition 2.** *If we neglect such adverse effects as reflections or multi-path*
 261 *(as we do in this context to keep our discussion neutral with respect to the*
 262 *adopted technology), the inspection of (10) and the results shown in [25] re-*
 263 *veal that the optimal deployment is simply given by a symmetric configuration*
 264 *with a distance d among the anchors.*

265 **Proposition 3.** *Considering again Equation (10), for a symmetric configu-*
 266 *ration of the anchors, the lowest GDoP is attained at the centre of the anchors*
 267 *configuration, i.e., $\underline{g} = g_n(\mathbf{p}_c)$.*

268 Given the centre $\mathbf{p}_c = [x_c, y_c]^T$ of the circle of radius δ upon which the
 269 anchors are deployed, in view of Proposition 2, the anchors will be deployed
 270 in the following position

$$\mathbf{a}_i = \mathbf{p}_c + \delta[\cos \theta_i, \sin \theta_i]^T, \quad (11)$$

271 where $\theta_i = 2i\pi/n$, $i = 1, \dots, n$, with the Euclidean distance between two
 272 adjacent anchors expressed using the 2-norm $\|\cdot\|$ being

$$d = 2\delta \sin(\pi/n) = \|\mathbf{a}_i - \mathbf{a}_{i+1}\|, \forall i \in \{1, \dots, n\}, \quad (12)$$

273 with the implicit assumption that $\mathbf{a}_{i+1} = \mathbf{a}_1$ for the periodicity of the circular
 274 deployment. Increasing the number n of anchors, will reduce their mutual

275 distance d (solid blue line in Figure 1), and will reduce the GDoP (Proposi-
 276 tion 1). Finally, the minimum GDoP will be attained in \mathbf{p}_c (Proposition 3).

277 By making the choice in (11) and considering a limited sensing range r ,
 278 we can choose \mathcal{P}_n as a symmetric region having the same centre \mathbf{p}_c as the
 279 anchor configuration. If we account for the limited sensing range, the area
 280 has to fall within the intersection of the circles centred in the anchors with
 281 radius r . As a result \mathcal{P}_n can be defined as

$$\mathcal{P}_n = \{\mathbf{p} \in \mathcal{P} | h_i(\mathbf{p}) \leq r \ \forall i \in \{1, \dots, n\} \wedge g_n(\mathbf{p}) \leq g^*\}, \quad (13)$$

282 where $n \geq 3$.

283 We can now formulate a few constraints stemming from purely geometric
 284 considerations.

- 285 • If $\delta > r$, it follows that $\mathbf{p}_c \notin \mathcal{P}_n$, which means that \mathbf{p}_c should be covered
 286 by additional anchors, hence a minimal deployment cannot be reached.
 287 If $\delta = r$ and $g_n(\mathbf{p}_c) \leq g^*$, we have $\mathbf{p}_c \equiv \mathcal{P}_n$, which is of course a non
 288 minimal configuration. Therefore, we will assume that $\delta < r$.
- 289 • If $\delta < r$ and $g_n(\mathbf{p}_c) > g^*$, in view of Proposition 3, we have $\mathcal{P}_n = \emptyset$.
 290 In this case, it is possible just to increase the number of anchors n
 291 deployed on the circle of radius δ up until we reach the condition $\mathcal{P}_n \neq$
 292 \emptyset . The GDoP equation (10) proves that this condition is achieved for
 293 a sufficiently large number of anchors (see Figure 1).
- 294 • Given $\delta < r$ and $g_n(\mathbf{p}_c) \leq g^*$, we have from (12) that $d < 2r$. The
 295 situation is the one displayed in Figure 2 for an example with $n = 3$.

296 Notice that since the GDoP depends only on the geometry of the deploy-
 297 ment, the value of the minimum GDoP $g_n(\mathbf{p}_c)$ for a fixed n does not change
 298 $\forall \delta > 0$. However, the region covered respecting the constraint $g_n(\mathbf{p}) \leq g^*$
 299 shrinks when δ decreases due to (10). On the other hand, since \mathcal{P}_n in (13) has
 300 to fall within the sensing range of all anchors, its maximum extension is given
 301 by the intersection of the n circles centred in the anchors, i.e., constrained by
 302 r (see the dark-solid shaded area in Figure 2). AS a consequence, the area
 303 jointly covered by the anchors shrinks when the anchors are pushed farther
 304 away by increasing δ , thus the anchors will be pushed outside the region \mathcal{P}_n .
 305 This is clearly visible in Figure 3 where we report

$$\mathcal{A}_n = \int_{\mathbf{p} \in \mathcal{P}_n} \mathbf{p} \, d\mathbf{p}, \quad (14)$$

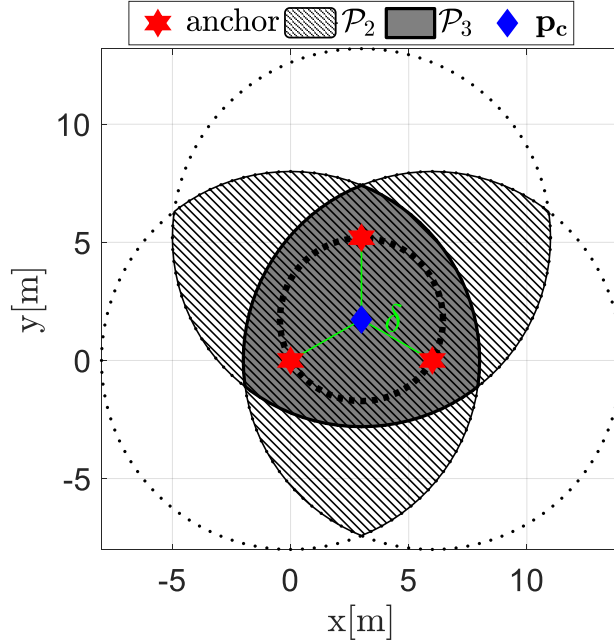


Figure 2: \mathcal{P}_3 region (solid fill) and \mathcal{P}_2 region (line pattern fill) with $r = 8$ [m] and $d = 0.75r$.

306 as a function of the distance d for fixed r ; However, since we are looking for
 307 the tile configuration that facilitates the coverage of the entire work-space by
 308 means of a set of overlapping tiles, it is convenient to consider configurations
 309 for which the anchors fall within \mathcal{P}_n , which implies $d < r$. By using (12),
 310 this choice implies:

$$\delta \leq \frac{r}{2 \sin(\pi/n)}. \quad (15)$$

311 A final fact needs to be stated on the point within the region \mathcal{P}_n that
 312 produces the worst (i.e., the maximum) GDoP. Assuming that the configura-
 313 tion is chosen so that \mathcal{P}_n contains all the n anchors (as per the previous
 314 observations) let

$$\mathcal{C}(a) = \{\mathbf{p} \in \mathcal{P} | \mathbf{p} = \mathbf{p}_c + a\delta[\cos \alpha, \sin \alpha]^T, \alpha \in [0, 2\pi)\}. \quad (16)$$

315 For $a > 1$ this is a circular region enclosing the circle where the anchors
 316 are deployed, e.g., it encloses the thick dotted line circle of radius δ in the
 317 example of Figure 2. By using (10), it is possible to show the following:

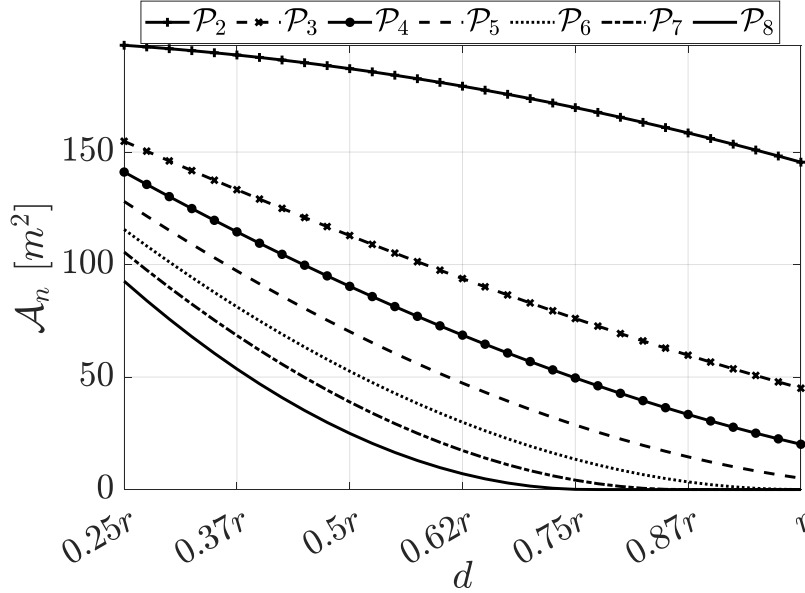


Figure 3: The coverage area for different number of anchors.

318 **Proposition 4.** Let $\mathcal{C}(a)$ be the region defined in (16) and let the con-
 319 figuration of the anchor be symmetric with respect to (15) (i.e., the an-
 320 chors fall inside \mathcal{P}_n). Let $\mathbf{p}_M(a) = \arg \max_{\mathbf{p} \in \mathcal{C}(a)} g_n(\mathbf{p})$, i.e. $g_n(\mathbf{p}_M(a)) =$
 321 $\max_{\mathbf{p} \in \mathcal{C}(a)} g_n(\mathbf{p})$. For small enough a and given (16), we have that $\mathbf{p}_M(a)$ is
 322 attained exactly by the angles

$$\alpha \in \left\{ \arctan \left(\frac{Y_1 - y_c}{X_1 - x_c} \right), \dots, \arctan \left(\frac{Y_n - y_c}{X_n - x_c} \right) \right\},$$

323 i.e., $\mathbf{p}_M(a)$ is along the direction from the centre \mathbf{p}_c to each of the anchors \mathbf{a}_i ,
 324 $i = 1, \dots, n$. This fact is true for any choice of δ respecting the hypotheses.

325 We observe that the result of Proposition 4 is strictly true only for small
 326 a , since, if a increases, the curves at constant GDoP tends to be circles, hence
 327 the GDoP has the same value on $\mathcal{C}(a)$ for any angle α . However, $\forall a > 1$
 328 and due to the anchors symmetric configuration, we have that the following
 329 holds always true

$$\mathbf{p}_M(a) = \left\{ \mathbf{p} \in \mathcal{C}(a) \mid \alpha = \arctan \left(\frac{Y_1 - y_c}{X_1 - x_c} \right) \right\}. \quad (17)$$

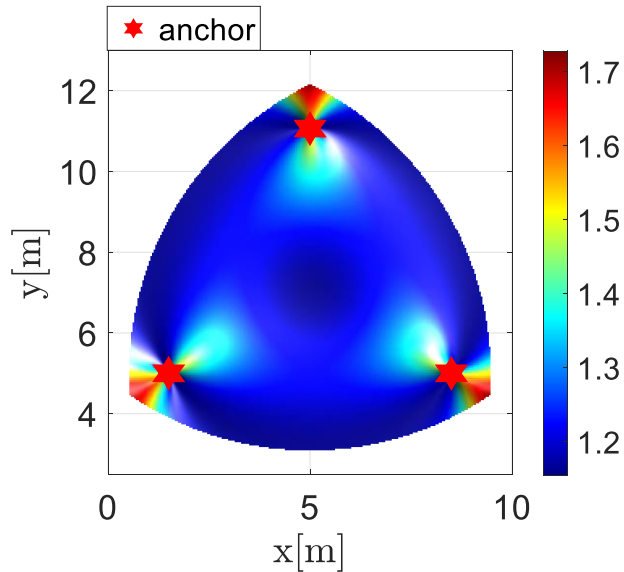


Figure 4: GDoP $g_3(\mathbf{p})$ surface with colour scale for \mathcal{P}_3 when $r = 8$ [m] and $d = 0.87r$.

330 *3.2. Example: \mathcal{P}_3 region*

331 It is known that in order to solve the position problem with ranging
 332 measurements (2) there should be at least $n = 3$ anchors in non-collinear
 333 configuration [23]. So it is very interesting to study the shape of the \mathcal{P}_3 re-
 334 gion. As shown in Figure 2 (dark-solid shaded region), if we use exactly three
 335 ranging measurements to reconstruct the target position, \mathcal{P}_3 is a circular tri-
 336 angle. The values of $g_3(\mathbf{p})$, i.e., the GDoP for $\mathbf{p} \in \mathcal{P}_3$, is graphically depicted
 337 in Figure 4 with a colour scale assuming $d = 0.87 r$. The geometric position
 338 estimation uncertainty $g_3(\mathbf{p})$ increases when the target moves towards the
 339 vertexes of the circular triangle (the intersection points among the circles
 340 centred in the three anchors with radius r), which are the locations of $\mathbf{p}_M(a)$
 341 given in Proposition 4.

342 *3.3. Anchor deployment for \mathcal{P}_n region*

343 After characterising the most important properties of our basic "tile" \mathcal{P}_n ,
 344 we are now in a condition to discuss Algorithm 1, which computes the op-
 345 timal tile and its anchor configuration. The algorithm takes as input the
 346 centre of tile \mathbf{p}_c , the sensing radius r and the target maximum uncertainty
 347 value expressed with the GDoP g^* . It returns the minimum number of an-
 348 chors needed to achieve the result and the radius δ of the circle they are to

Algorithm 1 Optimal anchor configuration

Input: central point \mathbf{p}_c , sensing radius r , desired g^*

Output: deployment radius δ , anchor number n

```
1:  $n = 3$ ;  $\delta = \langle \text{minimum possible value} \rangle$ ;  
2: flag = true  
3: do  
4:    $\underline{g} = g_n(\mathbf{p}_c)$   
5:   if  $\underline{g} \geq g^*$  then  $n = n + 1$   
6:   else flag = false  
7: while flag  
8: flag = true  
9: do  
10:   $\mathbf{a}_i = \mathbf{p}_c + \delta[\cos 2i\pi/n, \sin 2i\pi/n]^T, i = 1 \dots n$   
11:   $[p_M(a), a] = \text{find}_a(g^*)$   
12:  if  $p_M(a) == \emptyset$  then  $n = n + 1$   
13:  else flag = false  
14: while flag  
15: if  $n$  is even then  
16:    $\bar{\mathbf{a}} = \arg \max_{\mathbf{a} \in \mathbf{a}_i} |\mathbf{a} - \mathbf{p}_M(a)|$   
17:    $\delta = r/(a + 1)$   
18: else  
19:    $\bar{\mathbf{a}}_{1,2} = \arg \max_{\mathbf{a} \in \mathbf{a}_i} |\mathbf{a} - \mathbf{p}_M(a)|$   
20:    $d = r \left\| \frac{\mathbf{a}_1 - \mathbf{p}_M(a)}{\|\mathbf{a}_1 - \mathbf{p}_M(a)\|} - \frac{\mathbf{a}_2 - \mathbf{p}_M(a)}{\|\mathbf{a}_2 - \mathbf{p}_M(a)\|} \right\|$ ;  $\delta = \frac{\|\mathbf{a}_i^* - \mathbf{a}_j^*\|}{2 \sin(\pi/n)}$   
return  $\delta, n$ 
```

349 be deployed on using (11). The algorithm exploits the results on the charac-
 350 terisation of \mathcal{P}_n for symmetric configurations discussed above. The number
 351 of anchors is initially set to $n = 3$ (the minimum value). A first do-while
 352 loop increases n until the minimum value of the GDoP is less than g^* , which,
 353 in view of Proposition 3, is to be found at p_c independently of n . This loop
 354 exploits the monotonicity of GDoP with the number of anchors (Proposi-
 355 tion 1). The second do-while loop enforces the condition $g(\mathbf{p}_M(a)) \leq g^*$. To
 356 this end, it exploits a function find_a which looks for the smallest value of the
 357 scaling factor $a > 1$ such that the maximum GDoP $g(\mathbf{p}_M(a))$ evaluated on
 358 $\mathcal{C}(a)$ meets the constraints (see Proposition 4). If no point $\mathbf{p}_M(a)$ respecting
 359 the property exists, the loops considers a configuration with a greater number
 360 of anchors (notice that a solution surely exists by Proposition 1 and the
 361 fact that $g(\mathbf{p}_c) \leq g^*$). After the search is completed, we have to increase the
 362 deployment radius δ until the point $\mathbf{p}_M(a)$ falls inside the sensing range of
 363 the anchors (it is worth recalling that the position of $\mathbf{p}_M(a)$ does not depend
 364 on δ by Proposition 4). To this end the algorithm finds the anchor $\bar{\mathbf{a}}$ that,
 365 in the current configuration, is the farthest from $\mathbf{p}_M(a)$. If n is even there is
 366 only one $\bar{\mathbf{a}}$ and δ is given by $\frac{r}{a+1}$. If n is odd, we have two anchors $\mathbf{a}_{1,2}$ at
 367 the same distance from $\mathbf{p}_M(a)$. In this case, it is sufficient to compute the
 368 base length (which is the distance d) of an isosceles triangle with vertices in
 369 \mathbf{a}_1 , \mathbf{a}_2 and $\mathbf{p}_M(a)$, i.e., $d = r \left\| \frac{\mathbf{a}_1 - \mathbf{p}_M(a)}{\|\mathbf{a}_1 - \mathbf{p}_M(a)\|} - \frac{\mathbf{a}_2 - \mathbf{p}_M(a)}{\|\mathbf{a}_2 - \mathbf{p}_M(a)\|} \right\|$, and then compute δ
 370 reverting (12), i.e., $\delta = \frac{\|\mathbf{a}_1^* - \mathbf{a}_2^*\|}{2 \sin(\pi/n)}$.

371 Example of placements using the previous algorithm for $g^* = 1$ and $g^* =$
 372 0.9 are reported in Figure 5. In the first example, we have an odd number
 373 of anchors, resulting in $d = 0.59r$ and $\delta = 0.505r$, while in the second more
 374 stringent case we have an even number of anchors, resulting in $d = 0.55r$ and
 375 $\delta = 0.468r$, i.e. a more dense deployment, as consequence of the the higher
 376 performance required in terms of GDoP. Notice that the results are reported
 377 as a function of r since the graphs will be simply scaled for different values
 378 of r : Figure 5 reports an exemplifying value of $r = 20$ m. It is worthwhile
 379 to note that the cell for \mathcal{P}_5 and \mathcal{P}_6 are intersections of circles centred in the
 380 anchors positions (thick dashed lines in Figure 5). Finally, it is clear that
 381 with $n = 5$ we cannot ensure $g^* = 0.9$ (see the value of the level curves of
 382 $g_5(\mathbf{p})$ in Figure 5-a), unless a drastically reduced area (with anchors outside
 383 the deployment) is obtained. Hence, the minimum value needed is $n = 6$
 384 (Figure 5-b).

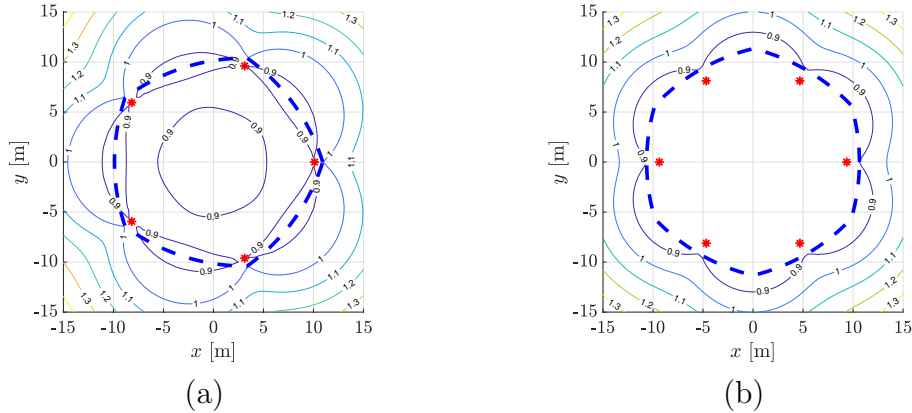


Figure 5: Placement when $r = 20$ m. The thick dashed line represents the cell contour, while the GDoP contour values for $g_5(\mathbf{p})$ (a) and $g_6(\mathbf{p})$ (b) are reported accordingly. The placement for $g^* = 1$ results in $d = 0.6r$ and $\delta = 0.5r$ (a), while for $g^* = 0.9$ with $d = 0.55r$ and $\delta = 0.47r$ (b).

385 4. Beyond \mathcal{P}_3 : the \mathcal{P}_2 case

386 The need to collect at least three anchor measurements is a geometric
 387 constraint, which is apparently impossible to surmount. The problem is very
 388 simple: if we use two anchors the point to localise can generally be in two
 389 different locations, corresponding to the intersection of two circles. This
 390 consideration leads us to define \mathcal{P}_3 as a subset of the intersection of the three
 391 circles within the sensing set of the three anchors. However, if we look for
 392 a coverage with minimal number of anchors that meets the target maximum
 393 uncertainty (maximum GDoP) we can work around this limitation. In the
 394 following, we first discuss how to define a basic tile out of three anchors,
 395 dubbed \mathcal{P}_2 , that covers a larger area than \mathcal{P}_3 (Section 4.1). Indeed, starting
 396 from \mathcal{P}_3 (intersection of three circles), \mathcal{P}_2 is obtained by adding the areas
 397 where only two circles intersect. As will be discussed in Section 4.2, in the
 398 areas of \mathcal{P}_2 we can still exploit our knowledge on the anchor positions to
 399 solve the ambiguity. Importantly, we will see in Section 4.3 that by using \mathcal{P}_2
 400 instead of \mathcal{P}_3 we can cover a larger area without sacrificing the worst case
 401 GDoP, i.e., still meeting the target maximum uncertainty requirement.

402 4.1. The \mathcal{P}_2 region

403 The region \mathcal{P}_2 is still defined using $n = 3$ anchors, but we release the
 404 assumption on their visibility requiring that at least three of them are simul-

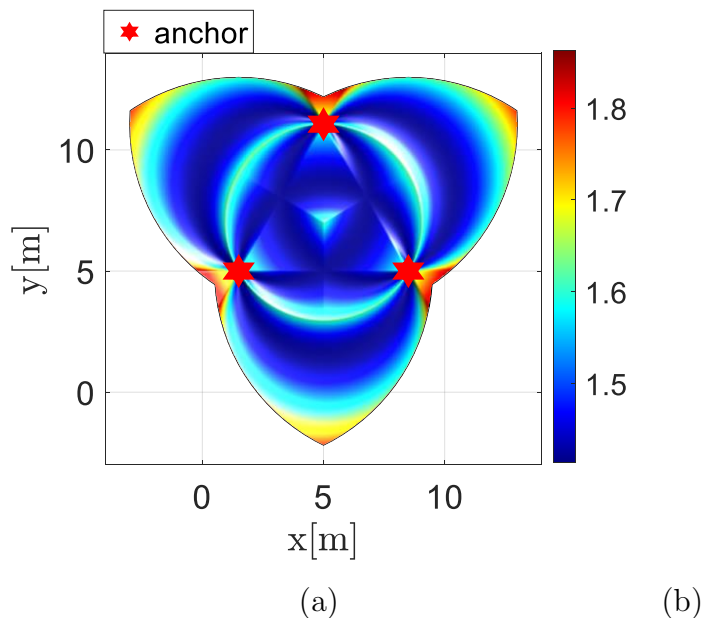


Figure 6: GDoP $g_2(\mathbf{p})$ surface with colour scale for \mathcal{P}_2 when $r = 8$ [m] and $d = 0.87r$.

405 taneously in sight. More formally, by handling (13), we have

$$\mathcal{P}_2 = \{\mathbf{p} \in \mathcal{P} | \exists i, j \in \{1, 2, 3\} \text{ s.t. } (h_i(\mathbf{p}) \leq r \wedge h_j(\mathbf{p}) \leq r) \wedge g_2(\mathbf{p}) \leq g^*\}.$$

406 The region \mathcal{P}_2 thus defined is exemplified in Figure 2, where it is covered with
 407 a linear pattern. The area covered by \mathcal{P}_2 is significantly larger than \mathcal{P}_3 (see
 408 Figure 3 or compare Figure 4 and Figure 6 for the same anchor deployment).
 409 The \mathcal{P}_2 region forms a three lens-shaped region. As can be observed from
 410 the corresponding GDoP plot of Figure 6, the target positioning uncertainty
 411 using two anchors increases at the circle intersections, while it reaches its
 412 highest value right behind each anchor, exactly as it happens for the \mathcal{P}_3 cells
 413 (recall Section 3.1).

414 4.2. Positioning with \mathcal{P}_2

415 Clearly, when a point lies at the intersection between the sensing circles
 416 of the three anchors, its position $\hat{\mathbf{p}}$ can be estimated using standard trilateration
 417 [24]. However, for the particular deployment we described for \mathcal{P}_2 ,
 418 $\hat{\mathbf{p}}$ can be estimated even with two anchors measurements. Considering the

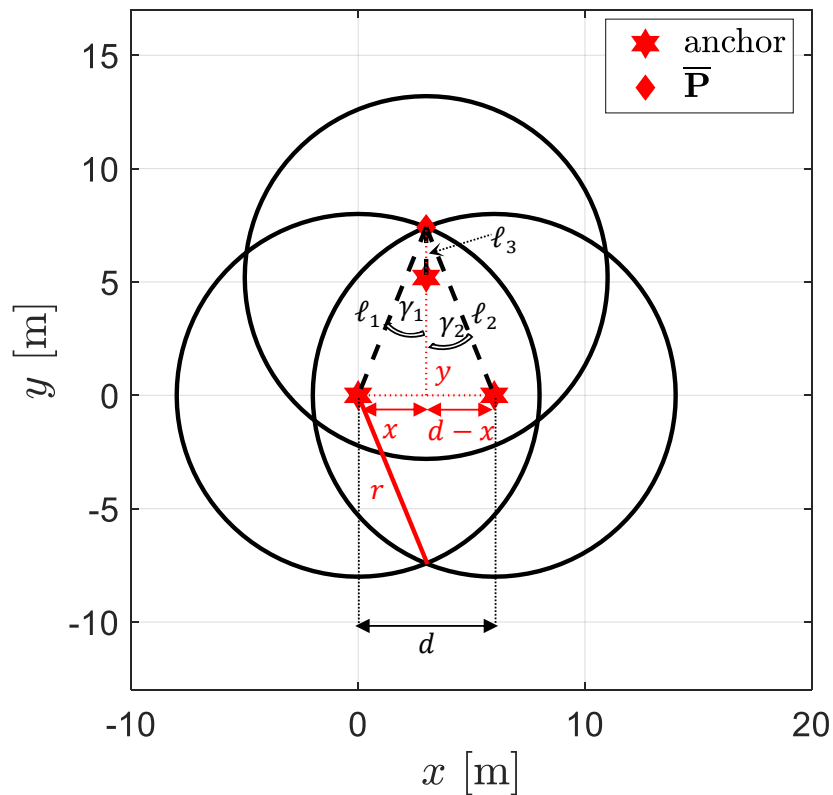


Figure 7: The geometry of the worst GDOP.

419 shaded area with line pattern fill in Figure 2, this condition occurs in the
 420 three areas not covered by the dark grey solid fill. Importantly, in each of
 421 these three regions, the pair of anchors in view are different and this infor-
 422 mation is available. Moreover, from any pair of anchors at distance d , say \mathbf{a}_i
 423 and \mathbf{a}_j , it is possible to express the position \mathbf{p} in a reference frame expressed
 424 in Figure 7 and dubbed \mathbf{p}^* using the following transformation

$$\mathbf{p}^* = \begin{bmatrix} \cos(\phi) & \sin(\phi) \\ -\sin(\phi) & \cos(\phi) \end{bmatrix} (\mathbf{p} - \mathbf{a}_i) = R(\phi) (\mathbf{p} - \mathbf{a}_i),$$

425 where $\phi = \arctan\left(\frac{Y_j - Y_i}{X_j - X_i}\right)$. With respect to this reference frame, the position
 426 \mathbf{p} given two ranging measurements is given by

$$\mathbf{p}^* = \begin{bmatrix} \frac{d^2 - \ell_j^2 - \ell_i^2}{2d} \\ \pm \sqrt{\frac{4d^2 \ell_i^2 - (d^2 - \ell_j^2 + \ell_i^2)^2}{4d^2}} \end{bmatrix},$$

427 hence expressing the ambiguity along the y direction. As a consequence,

$$\mathbf{p} = R(\phi)^T \mathbf{p}^* + \mathbf{a}_i. \quad (18)$$

428 It is now evident that there are two locations for \mathbf{p} , which are symmetric with
 429 respect to the segment passing through \mathbf{a}_i and \mathbf{a}_j . With respect to Figure 2,
 430 it follows that either \mathbf{p} is in the shaded dark grey area or in the line pattern
 431 fill, condition that can be easily verified by the presence or not of the third
 432 ranging measurement. As such, there is no ambiguous location for the \mathcal{P}_2
 433 cell. Since the estimated location $\hat{\mathbf{p}}$ is given by the NWLS applied to the \mathcal{P}_2
 434 cell, we dubbed this solution algorithm as NLS.

435 **Remark 1.** *The possibility of resolving the ambiguity is subject to some geo-*
 436 *metric conditions. Indeed, when $d \leq r$, the ambiguous location can be always*
 437 *uniquely determined by the presence or absence of third anchor measurement*
 438 *(see Figure 8 (a)). On the other contrary, if $d > r$, it is possible to have am-*
 439 *biguities (see Figure 8 (b)). Notice that, as discussed in Section 3.1, the fact*
 440 *that the anchors fall within \mathcal{P}_n , implies $d < r$, hence no ambiguous locations*
 441 *exist.*

442 **Remark 2.** *The presence or absence of the third measurement, is instru-*
 443 *mental to set up the NWLS in (3)-(5). Indeed, since that is a gradient*
 444 *descent-like algorithm, if the initial location is set at the centre of the re-*
 445 *gion with line pattern fill or in the dark grey shaded area of Figure 2, the*
 446 *algorithm will inevitably converge towards the correct location.*

447 4.3. Positioning uncertainty in \mathcal{P}_2 and \mathcal{P}_3 cells

448 As discussed in Section 3 (Proposition 1) for a fixed distance d between
 449 the anchors the GDoP improves with the number n of anchors. Hence, \mathcal{P}_3
 450 yields a smaller GDoP value than \mathcal{P}_2 . Nonetheless, we will now show that
 451 given a generic \mathcal{P}_3 , it is possible to define \mathcal{P}_2 such that $\max_{\mathbf{p} \in \mathcal{P}_2} g_2(\mathbf{p}) =$
 452 $\max_{\mathbf{p} \in \mathcal{P}_3} g_3(\mathbf{p})$ with a larger area covered by \mathcal{P}_2 . However, we will have to
 453 allow for a slightly larger distance between the anchors in \mathcal{P}_2 than in \mathcal{P}_3 .

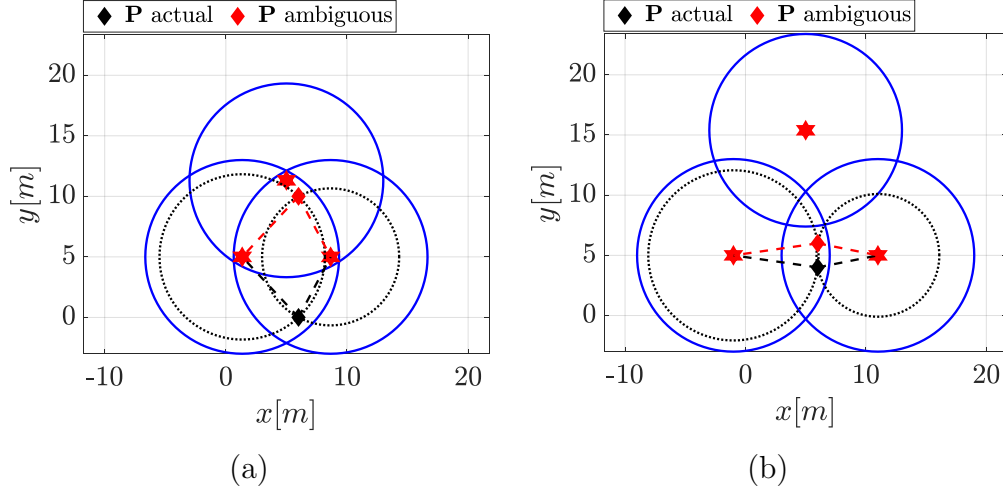


Figure 8: The necessary condition for \mathcal{P}_2 to resolve the ambiguity in position estimation using two anchors.

454 **Theorem 1.** *For any \mathcal{P}_3 cell with $d \leq r$, there exists a \mathcal{P}_2 cell such that*
 455 *$\max_{\mathbf{p} \in \mathcal{P}_2} g_2(\mathbf{p}) = \max_{\mathbf{p} \in \mathcal{P}_3} g_3(\mathbf{p})$ as defined in (10) and having $\mathcal{A}_2 \geq \mathcal{A}_3$ as*
 456 *defined in (14). The distance between the anchors is βd , with¹:*

$$\beta = \sqrt{\xi \pm \sqrt{\xi^2 - 2\xi + \frac{2}{3}}} \text{ and } \xi = \frac{2r^2}{d^2}. \quad (19)$$

457 **PROOF.** Without loss of generality, let us consider the anchors are deployed
 458 as in (11) and located at

$$\mathbf{a}_1 = \begin{bmatrix} 0 \\ 0 \end{bmatrix}, \mathbf{a}_2 = \begin{bmatrix} d \\ 0 \end{bmatrix} \text{ and } \mathbf{a}_3 = \begin{bmatrix} d \cos \pi/3 \\ d \sin \pi/3 \end{bmatrix},$$

459 i.e., the vertices of an equilateral triangle, which is the configuration for three
 460 anchors discussed in Section 3. Consider the point corresponding to the
 461 maximum GDoP $\bar{\mathbf{p}}_{M_i} = [x, y]^T \in \mathbf{p}(a)$ defined in (17) for the i -th cell \mathcal{P}_i , i.e.,
 462 the locations $\bar{\mathbf{p}}_{M_2}$ and $\bar{\mathbf{p}}_{M_3}$ with maximum GDoP given by the intersection
 463 of two and three circles, respectively, of radius r (see Figure 7). Considering
 464 that the anchors for \mathcal{P}_2 are at distance βd , with d being their distance for

¹Albeit negative solutions for β exists, they have no physical meaning.

465 \mathcal{P}_3 . We can compute the explicit GDoP in the two points applying (10):

$$\begin{aligned}
 g_3(\bar{\mathbf{p}}_{M_3}) &= \sqrt{\frac{3}{\sum_{i=1}^{i=2} \sum_{j=i+1}^{j=3} \sin(\gamma_i - \gamma_j)^2}} = \sqrt{\frac{3r^4}{y^2d^2 + 2r^2x^2}}, \\
 g_2(\bar{\mathbf{p}}_{M_2}) &= \sqrt{\frac{2r^4}{y^2\beta^2d^2}}.
 \end{aligned}
 \tag{20}$$

466 By imposing $g_2(\bar{\mathbf{p}}_2) = g_3(\bar{\mathbf{p}}_3)$ and solving for β , we have the following two
 467 roots

$$\beta = \sqrt{\xi \pm \sqrt{\xi^2 - 2\xi + \frac{2}{3}}} \text{ and } \xi = \frac{2r^2}{d^2},
 \tag{21}$$

468 yielding non-complex values for $r > 0$ and $d \leq r$, with two positive roots.

469 The last step to complete the proof is to show that, by setting the distance
 470 between the anchors in \mathcal{P}_2 to βd , we have $\mathcal{A}_2 \geq \mathcal{A}_3$. \mathcal{A}_2 is obviously larger
 471 than \mathcal{A}_3 when the anchors are deployed at the same distance (see Figures 3).
 472 When the anchors for \mathcal{P}_2 are deployed at distance βd , the area covered by
 473 \mathcal{A}_2 decreases by increasing β . It can be seen that for any choice of $r > 0$ and
 474 $d \leq r$, we have $\mathcal{A}_2 > \mathcal{A}_3$, if $\beta \leq 1.7$ (see [30]). It can be seen that for any
 475 value of ξ in (19), one of the two solutions for β is always smaller than 1.7.
 476 Therefore, it is possible to find a region \mathcal{A}_2 greater than \mathcal{A}_3 and with equal
 477 worst case GDoP.

478 **Remark 3.** *The cell \mathcal{P}_2 constructed as discussed in Theorem 1 is guaranteed*
 479 *to have the same worst case GDoP and a better coverage than the correspond-*
 480 *ing \mathcal{P}_3 . The price to pay is that the GDoP (and hence the uncertainty) can*
 481 *be worse in the average. Indeed, the uncertainty of the estimates degrades*
 482 *when the target lays on the line pattern filled area of Figure 2.*

483 **Remark 4.** *The value $\beta = 1.7$ is actually an upper bound for the "legal"*
 484 *ranges of β , i.e., the ones that guarantee $\mathcal{A}_2 \geq \mathcal{A}_3$. We know that this*
 485 *bound is actually conservative and we are currently looking for the tightest*
 486 *possible bound that guarantee this geometric property. In the next section,*
 487 *we empirically obtain an approximate value for this bound, which we define*
 488 *as the "approximate optimal bound for positioning uncertainty" in \mathcal{P}_2 .*

489 5. Simulation Results

490 As a first goal, we aimed for a numeric comparison between \mathcal{P}_2 and \mathcal{P}_3
491 cell geometry. The comparison was made on the efficiency gain (i.e., number
492 of anchors needed) and on the positioning accuracy. Since an experimental
493 comparison would have required a massive deployment of anchors, we decided
494 to use simulation data. The reader interested in an accurate evaluation of
495 the trilateration uncertainty adopting as ranging sensors UWB anchors is
496 referred to our previous work [25].

497 We considered a simulated map generated by the Robotics System Tool-
498 box of Matlab R2020a Software with the total coverage area of $557 m^2$. We
499 have considered the maximum sensing range to be $r = 8$ m and a maxi-
500 mum GDOP value of $g^* = 1.98$, which resulted in an anchor distance of
501 $d = 6$ m for the \mathcal{P}_3 cell. With the same constraints, the anchor distance for
502 the \mathcal{P}_2 obtained with the scaling parameter β in (19) was given by $d = 6.2$ m
503 ($\beta = 1.03$).

504 For the deployment results, since we have fully characterised the regions
505 $\mathcal{P}_j \subseteq \mathcal{P}$ so that the limited sensing range r is satisfied and $g_j(\mathbf{p}) \leq g^*$,
506 $\forall \mathbf{p} \in \mathcal{P}_j$, it is sufficient to cover the entire space \mathcal{P} with regions \mathcal{P}_j to ensure
507 $g(\mathbf{p}) \leq g^*$, $\forall \mathbf{p} \in \mathcal{P}$. The geometric parameters for the deployment of the
508 anchors were obtained using Algorithm 1.

509 5.1. Ranging anchors deployment

510 The anchor deployment problem as defined here with geometric cells (be
511 them \mathcal{P}_2 or \mathcal{P}_3) is a special case of the general class of covering problems [31,
512 32, 21], where a space \mathcal{P} is fully covered with cells (or tiles) of a given
513 geometry. As shown in [33], the optimal covering of a plane with convex
514 polygons is an NP-Complete problem. Unfortunately, this negative result is
515 obviously applicable to the cell geometry considered in this paper.

516 However, the coverage problem considered in this paper can be approached
517 adapting the solutions proposed in the literature. For example, a basic so-
518 lution for NP-Complete covering problems (e.g., vertex cover, hitting set,
519 general set cover, geometric set cover, etc.) is the greedy heuristic vertex
520 covering algorithm proposed by Hochbaum et al. [34]. This approach pro-
521 duces an upper bound for the number of tiles (and hence of anchors) needed
522 for the coverage and has a logarithmic approximation ratio [35]. As discussed
523 next, the covering greedy algorithm in general produces a solution that is not
524 in practice too far from the optimal.

525 In our example, an initial set of 6000 random cells in equilateral triangle
 526 patterns was generated uniformly inside the region of interest. By using the
 527 greedy approximation algorithm with \mathcal{P}_3 cells, the result is 12 cells deployed
 528 with a maximum coverage area of 529 m² and with a total computation
 529 time of 682.5 s. On the other hand, by using \mathcal{P}_2 cells, the coverage area
 530 was larger, i.e., 552 m², while the computation time was smaller (416 s) and
 531 the algorithm used significantly less cells than in the case of \mathcal{P}_3 , i.e., just 5.
 532 These results were obtained in MathWorks Matlab R2022b software running
 533 in Microsoft Windows 10, and using a 2.60 GHz Intel(R) Core(TM) i7 micro-
 534 processor endowed with 16 GB RAM. The two deployment are reported in
 535 Figure 9 and Figure 10, respectively. By looking at the deployment results,
 536 it appears that the the final solution does not provide a full coverage for
 537 the map. This is a common problem when heuristic solutions are applied to
 538 complex environments. Leaving some parts of the map uncovered is often
 539 preferable over using an unnecessarily large number of anchors. However,
 540 this problem is solved by placing anchors strictly were needed at the end of
 541 the algorithm.

542 5.2. Positioning results

543 The previous section clearly shows evident advantages in the covering
 544 performance of using \mathcal{P}_2 over \mathcal{P}_3 . Our goal is now to show the performance
 545 of the two tiles in terms of positioning uncertainty. For this test, we assumed
 546 that the ranging uncertainty η_i in (2) was the same for all anchors and was
 547 distributed according to a Gaussian, white, zero-mean stochastic process with
 548 a standard deviation of σ_ℓ . The cell geometry for \mathcal{P}_2 and \mathcal{P}_3 considered for
 549 this test are the one shown in Figure 11. For all the tests, we assumed a
 550 fixed sensing range of $r = 10$ m was used. For \mathcal{P}_2 , the position estimates are
 551 found using the algorithm described in Section 4.2 and the NWLS described
 552 in (3)-(5). The corresponding solution for the \mathcal{P}_3 is given by the GWLS
 553 method [25], which is hence adopted. Notice that, as reported in [25], this
 554 will ensure the attainment of the CRLB: to further verify this fact, we also
 555 reports the solution for \mathcal{P}_3 when the simple Least Squares (LS) is adopted.

For each position in the grid cell, we collected the position estimation
 error for $m = 1000$ Monte Carlo (MC) simulations. This procedure was
 repeated with three different measurement standard uncertainties, namely
 $\sigma_\ell = [0.05, 0.1, 0.2]$ m. The results are reported in Figure 12 for all the
 estimation algorithms described above. For the positioning estimation un-
 certainty, the quantitative results in terms of the Root Mean Square Error

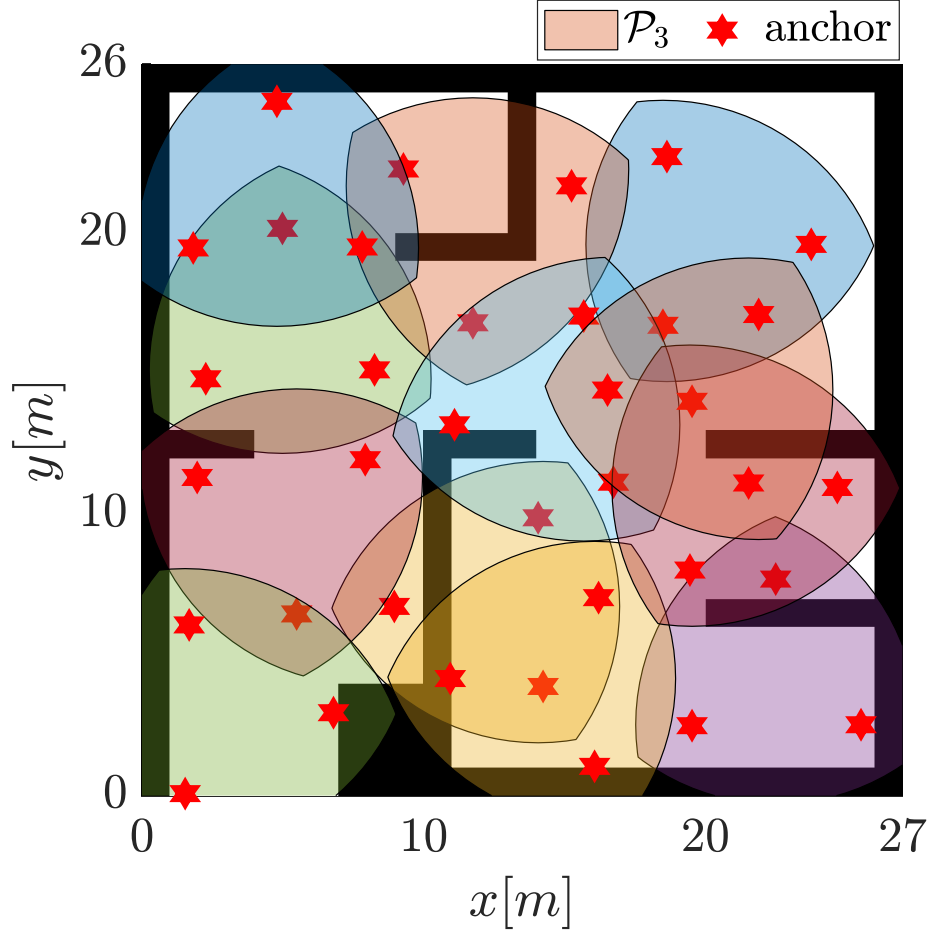


Figure 9: The final deployed anchors for the \mathcal{P}_3 cells.

(RMSE) were used, i.e.

$$\text{RMSE}_{\mathbf{p}} = \sqrt{\frac{1}{mN} \sum_{i=1}^N \sum_{j=1}^m \frac{(x_i - \hat{x}_{i,j})^2 + (y_i - \hat{y}_{i,j})^2}{2}}$$

556 where N is the number of grid points in the grid cell, $\mathbf{p}_i = [x_i, y_i]^T$ are the i -th
 557 actual coordinates of the grid cell and $\hat{\mathbf{p}}_{i,j} = [\hat{x}_{i,j}, \hat{y}_{i,j}]^T$ are the corresponding
 558 estimated coordinates of the i -th grid cell point for the j -th MC simulation.
 559 The results of Figure 12 shows that the GWLS surely provides results that
 560 are better than LS for the \mathcal{P}_3 regardless of the distances d among the anchors

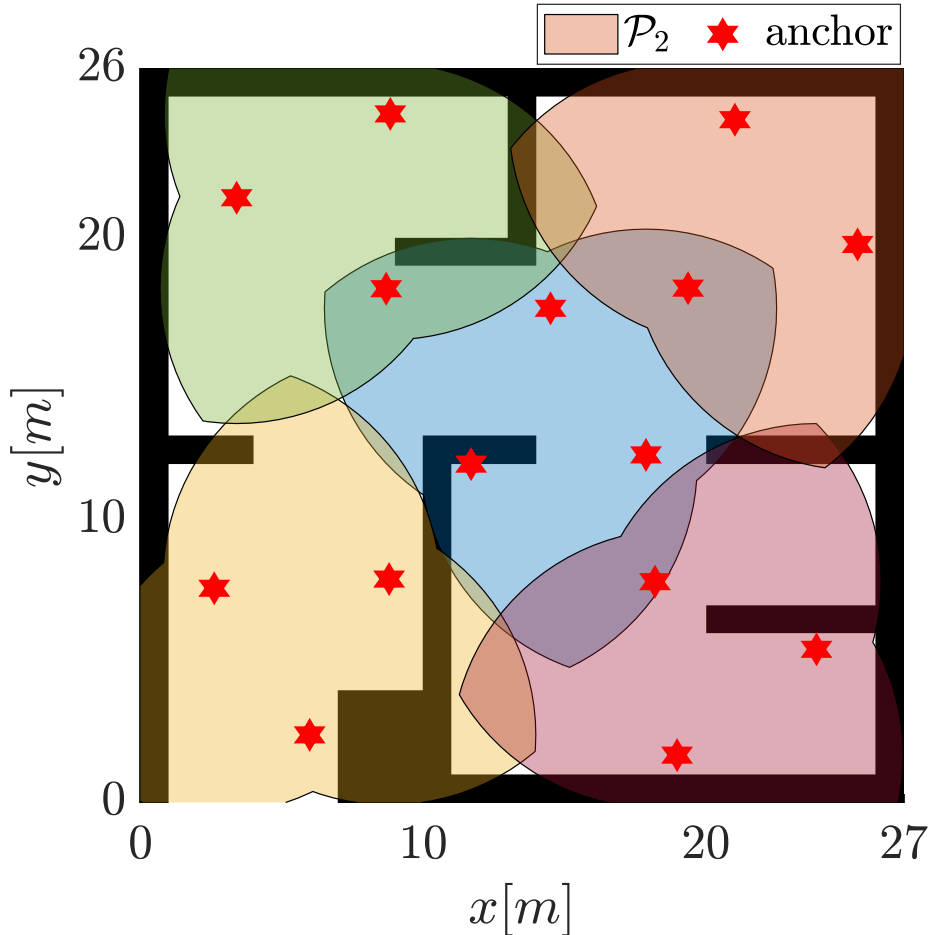


Figure 10: The final deployed anchors for the \mathcal{P}_2 cells.

561 and in all the locations on the plane that are covered by the three anchors (see
 562 Figure 11-c). We additionally report with a solid line in Figure 12 the RMSE
 563 for all the points in \mathcal{P}_2 (say RMSE_2) when the distance $d_2 = r = 10$ m (grid of
 564 Figure 11-a), used as comparison. This RMSE reports the error between the
 565 true target position and the estimated value using NLS, i.e., the intersection
 566 point of two ranging measurements in \mathcal{P}_2 described in Section 4.2. We then
 567 notice that when $d \geq \gamma d_2 = 6.36$ m, (vertical line in Figure 12) the RMSE
 568 for all the points in the region \mathcal{P}_3 (say RMSE_3) is smaller than RMSE_2 .
 569 However, from Theorem 1, we know that there exists a value of $\beta \geq 1.7$ such
 570 that for $d_2 = \beta d$ we have that $\mathcal{A}_2 \geq \mathcal{A}_3$ with the same maximum GDoP.

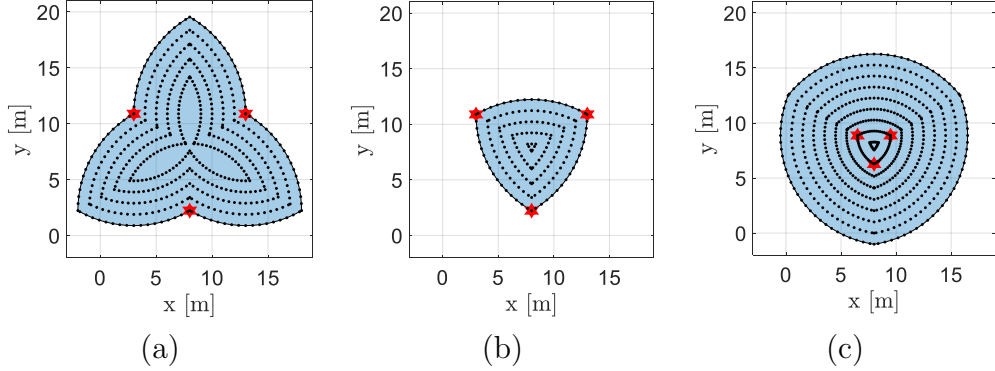


Figure 11: Three sample grid cells with $r = 10$ [m]. (a) \mathcal{P}_2 with $d = r$, (b) \mathcal{P}_3 with $d = r$, and (c) \mathcal{P}_3 with $d = 0.3r$.

571 Therefore, we have that if $1 < \beta < 1/\gamma = 1.57$, then the $\text{RMSE}_3 < \text{RMSE}_2$,
 572 while if $1/\gamma \leq \beta \leq 1.7$, then $\text{RMSE}_3 \geq \text{RMSE}_2$, which is our "approximate
 573 optimal bound for positioning uncertainty" for \mathcal{P}_2 .

574 6. Experimental Results

575 The arena considered for the experiment is the IoT laboratory of the
 576 Department of Information Engineering and Computer Science (DISI), Uni-
 577 versity of Trento, a 6×6 m² area instrumented with an OptiTrack system
 578 equipped with 14 cameras that provides the ground truth data (i.e., the
 579 precise location of the anchors in this experiment). We adopted as ranging
 580 sensors anchors based on radio frequency technology, namely UWB nodes.

581 Hence, the target and the testing area are instrumented with DecaWave
 582 UWB transceivers (see Figure 13) with DWM1001 module, which includes a
 583 DWM1000 UWB transceiver (compliant with the IEEE802.15.4 UWB phys-
 584 ical layer), a Nordic Semiconductor nRF52832 micro-controller unit (MCU)
 585 with Bluetooth low Energy (BLE) support, and a three-axis accelerometer.
 586 The module operates on 6 frequency bands with base frequencies ranging
 587 from 3.5 to 6.5 GHz and a bandwidth of 500 or 900 MHz working with a
 588 two-way-ranging-TOA (TWR-TOA) protocol for an asynchronous commu-
 589 nication. In addition to the anchors of the infrastructure, the setup comprises
 590 one tag as the target, whose position is to be estimated and linked to a laptop,
 591 and one anchor configured as initiator to configure the DRTLS network. To
 592 prevent interference, a channel access time division multiple access (TDMA)
 593 is used to enforce collision-free signal broadcasting from different anchors. In

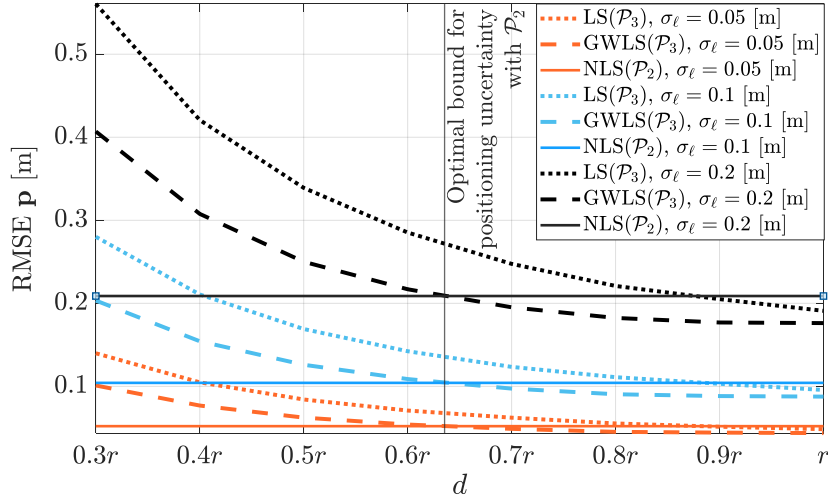


Figure 12: RMSE vs d for the \mathcal{P}_2 and the along the grid points of Figure 11, for the different estimation algorithms employed and with different distances between the anchors for \mathcal{P}_3 .

594 agreement with the IEEE802.15.4 standard, the initiator starts the TDMA
595 cycle for a TWR communication and keeps the clocks of the anchors synchro-
596 nised. The tag communicates with each anchor within a 25 ms time interval
597 that results in a positioning network system with 10 Hz sampling rate (i.e.,
598 one 25 ms slot is allotted to the Initiator) for the total communications and
599 measurements of the whole positioning network system.

600 The UWB measurement results were collected using three anchors pre-
601 cisely located in an equilateral triangular pattern using the OptiTrack system
602 (having an expanded uncertainty of 1 mm) and placed at 1683 mm off the
603 floor (see Figure 13). The anchors are placed under line-of-sight (LOS) con-
604 ditions. However, to ensure realistic environmental conditions, the lab was fully
605 furnished and equipped with several laboratory instruments. The inevitable
606 reflections by the walls, ceiling and different furniture, majorly made of metal
607 in the lab, caused undesired signal interference and attenuation, resulting in
608 biases in the signal time of arrival. This phenomenon is depicted in the two
609 sample measurement error probability mass functions (pmf) obtained from
610 two different UWB anchors and in two different locations on the experimen-
611 tal environment and depicted in Figure 14. Considering a Type A analysis,
612 we collected ranging measurements at the maximum positioning frequency,
613 i.e. 40 Hz per anchor. The pmfs represent the ranging measurement errors:
614 they were computed by subtracting the actual distance (i.e., the ground truth

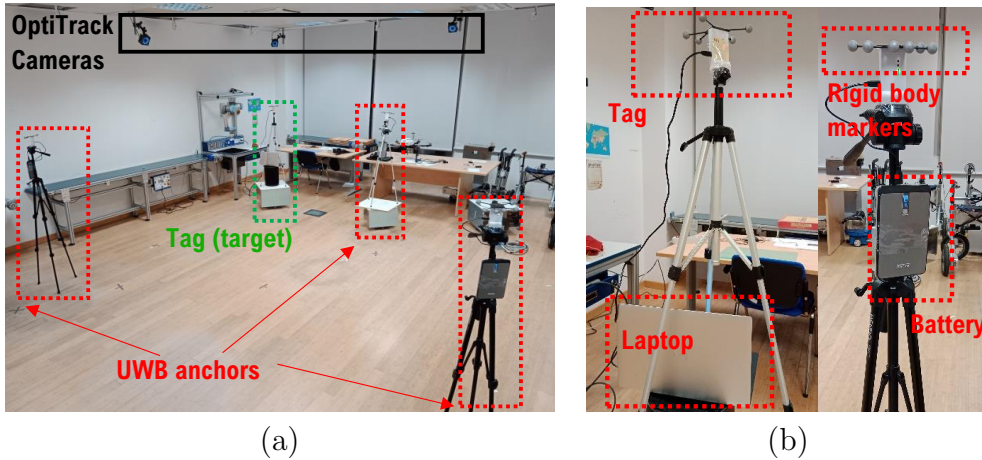


Figure 13: Experimental setup with DecaWave MDEK UWB positioning system. (a) The overview of the arena, and (b) the experimental setup.

615 distance from stationary target to the UWB anchors retrieved from the Op-
 616 tiTrack system with millimetre accuracy) from the 900 measurement results
 617 received from the UWB anchor. From the analysis carried out from two
 618 different anchor locations, we observed that the UWB measurements are su-
 619 perimposed with an uncertainty that has standard deviation of $\sigma_\ell = 0.1$ m
 620 and a positive/negative maximum bias ranging in the set ± 0.28 cm. The
 621 experiment consists of two different equilateral triangular deployment with
 622 four sampled locations, all depicted in Figure 15. In the first scenario, Fig-
 623 ure 15-a, the anchors were located with the same distance $d = 2.59$ m for \mathcal{P}_2
 624 and \mathcal{P}_3 . In the second scenario, the distances between the anchors in \mathcal{P}_2
 625 was extended by choosing $\beta = 1.62$, a value close to the optimal bound which
 626 was empirically obtained in Section 5 and that has a minimal increase in the
 627 covered area but a large average reduction of GDoP. For each position on
 628 the map, 900 estimates were made for \mathcal{P}_2 and \mathcal{P}_3 . The GDoP (calculated
 629 by the ground truth measurements retrieved by the OptiTrack system) and
 630 RMSE results (computed as in Section 5) are reported in Table 1 and Ta-
 631 ble 2, respectively. From Table 1 we can observe how the GDoP in the same
 632 exact locations decreases when the distance among the anchors increases.
 633 Moreover, when the distance is the same, \mathcal{P}_2 conveys a GDoP that is greater
 634 than \mathcal{P}_3 , thus verifying that $\beta > 1$ in light of Theorem 1. Moreover, when
 635 β increases, we can observe a reduction of the GDoP \mathcal{P}_2 , but at the price
 636 of a reduced area covered \mathcal{A}_2 (see Figure 15). From Table 2, we can notice

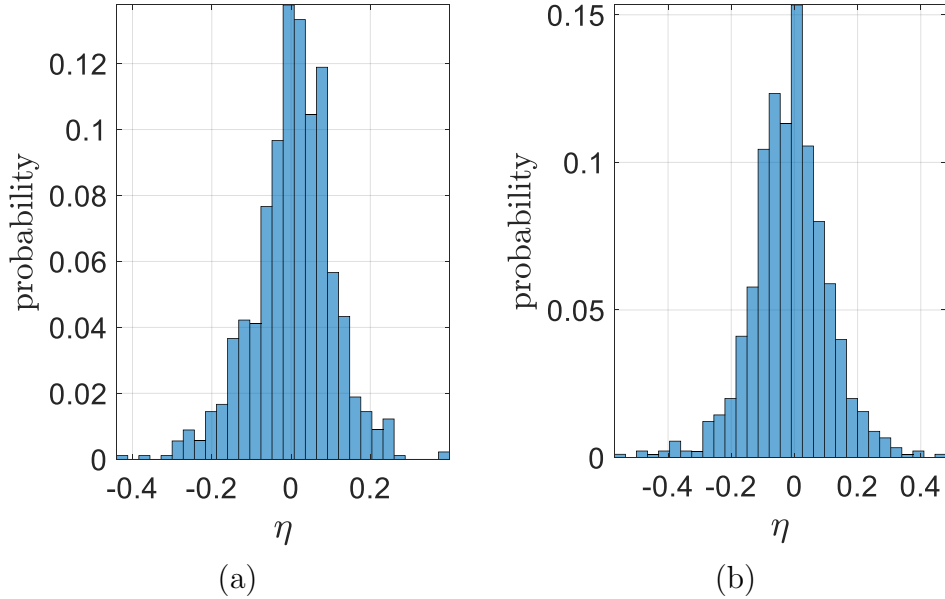


Figure 14: Two sample measurement error pmfs obtained from two different UWB anchors and in two different locations on the experimental environment, with (a) positive and (b) negative bias.

637 that with the adopted $\beta = 1.62$, we have a smaller average positioning error
 638 for \mathcal{P}_2 with respect to \mathcal{P}_3 , while still preserving a larger coverage area (see
 639 Figure 15-b), which is in perfect accordance with the numerical analysis of
 640 Section 5. Finally, from both the tables, we can notice that the RMSE and
 641 the GDoP follow the same exact patterns, i.e., when the GDoP of \mathcal{P}_2 is less
 642 than \mathcal{P}_3 so does the RMSE, and vice-versa, which empirically validates once
 643 our choice of choosing the GDoP to meet the target uncertainty.

644 7. Conclusion

645 In this paper, we have presented a novel solution for an algorithm that
 646 produces a large scale deployment for ranging sensors so that a few impor-
 647 tant requirements are respected. The requirements are of theoretical nature
 648 and practical nature and include scalability, generality, optimality, reliabil-
 649 ity and ability to deal with the physical limitations of the sensors (first and
 650 foremost the limited sensing range). We have proposed a two step algorithm
 651 in which first a basic cell structure (or tile) is designed and optimised to
 652 cover a specified area with guaranteed compliance with the desired target

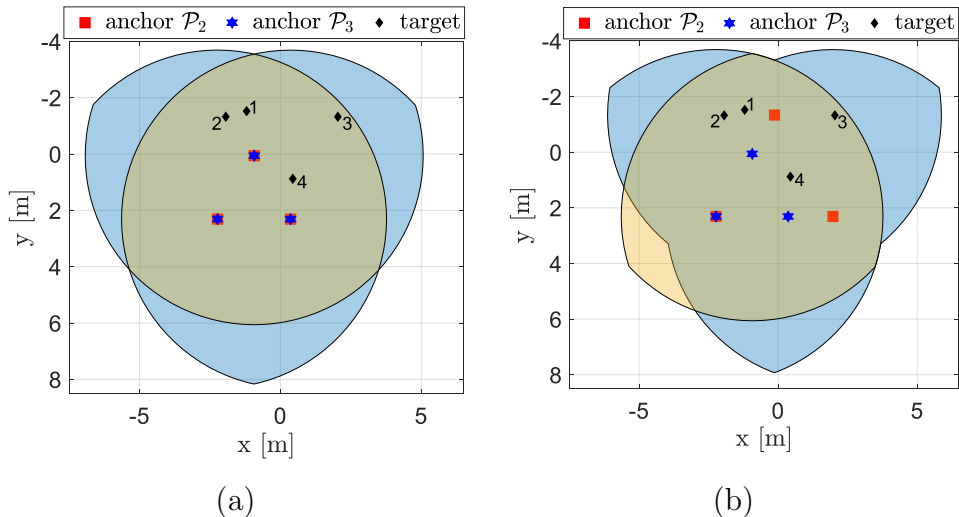


Figure 15: Experimental positioning locations (numbered 1 to 4) and two different anchor deployments. (a) \mathcal{P}_2 and \mathcal{P}_3 with the same $d = 2.59$ m (b) \mathcal{P}_2 with $d = 4.20$ m and \mathcal{P}_3 with $d = 2.59$ m.

Table 1: GDoP values for the four different positions and the two configurations of Figure 15.

Target	\mathcal{P}_3	\mathcal{P}_2 ($d = 2.59$) [m]	\mathcal{P}_2 ($d = 4.20$) [m]
1	2.260	2.338	1.419
2	1.947	2.168	1.419
3	2.126	2.190	1.414
4	1.454	1.596	1.455

653 uncertainty, and then this structure is replicated in order to cover the entire
654 space. The key contributions of the paper have been to show: the geometric
655 properties of the cell, an algorithm to design it with a minimal symmetric
656 configuration of anchors, and how the covering efficiency can be maximised
657 when the number of anchors is chosen as the smallest (i.e., $n = 3$).

658 A large amount of work is still ongoing or is reserved for future investiga-
659 tions. One issue we are coping with is the extension of the proposed analysis
660 with heterogeneous sensing range and to the three/dimensional case. Another
661 direction of work is to study how the proposed results extend to localisation
662 problems and how the cells may be modified still verifying the target uncer-
663 tainty (this is relevant to adapt the cells to challenging scenarios). Finally,
664 we are going to extend the analysis to more complicated uncertainty models

Table 2: RMSE values for the four different positions and the two configurations of Figure 15 with the algorithms described in Section 5.

Target	$\mathcal{P}_3(\text{LS})$	$\mathcal{P}_3(\text{GWLS})$	$\mathcal{P}_2(d = 2.59)$ [m]	$\mathcal{P}_2(d = 4.20)$ [m]
1	0.179	0.123	0.145	0.096
2	0.179	0.111	0.133	0.095
3	0.218	0.143	0.150	0.111
4	0.090	0.076	0.15	0.096

665 that considers the effect of the environment generating multipath and biases,
 666 considering both model-based and data-driven approaches as [36, 37].

667 References

- 668 [1] D. Fontanelli, Perception for Autonomous Systems: A Mea-
 669 surement Perspective on Localisation and Positioning, IEEE
 670 Instrumentation Measurement Magazine 25 (4) (2022) 4–9.
 671 doi:10.1109/MIM.2022.9777773.
- 672 [2] A. Filgueira, H. González-Jorge, S. Lagüela, L. Díaz-Vilariño, P. Arias,
 673 Quantifying the influence of rain in LiDAR performance, Measurement
 674 95 (2017) 143–148.
- 675 [3] N. Ahmed, S. S. Kanhere, S. Jha, On the importance of link charac-
 676 terization for aerial wireless sensor networks, IEEE Communications
 677 Magazine 54 (5) (2016) 52–57.
- 678 [4] G. Bellusci, G. J. M. Janssen, J. Yan, C. C. J. M. Tiberius, Model of
 679 distance and bandwidth dependency of TOA-based UWB ranging error,
 680 in: IEEE International Conference on Ultra-Wideband, Vol. 3, 2008, pp.
 681 193–196. doi:10.1109/ICUWB.2008.4653448.
- 682 [5] N. A. Alsindi, B. Alavi, K. Pahlavan, Measurement and Modeling of
 683 Ultrawideband TOA-Based Ranging in Indoor Multipath Environments,
 684 IEEE Transactions on Vehicular Technology 58 (3) (2009) 1046–1058.
 685 doi:10.1109/TVT.2008.926071.
- 686 [6] V. Magnago, L. Palopoli, R. Passerone, D. Fontanelli, D. Macii, Effec-
 687 tive Landmark Placement for Robot Indoor Localization with Position

- 688 Uncertainty Constraints, *IEEE Trans. on Instrumentation and Measure-*
689 *ment* 68 (11) (2019) 4443–4455. doi:10.1109/TIM.2018.2887071.
- 690 [7] P. Nazemzadeh, D. Fontanelli, D. Macii, Optimal Placement of
691 Landmarks for Indoor Localization using Sensors with a Limited
692 Range, in: *International Conference on Indoor Positioning and*
693 *Indoor Navigation (IPIN)*, IEEE, Madrid, Spain, 2016, pp. 1–8.
694 doi:10.1109/IPIN.2016.7743631.
- 695 [8] A. E. Redondi, E. Amaldi, Optimizing the placement of anchor nodes
696 in rss-based indoor localization systems, in: *2013 12th Annual Mediter-*
697 *anean Ad Hoc Networking Workshop (MED-HOC-NET)*, IEEE, 2013,
698 pp. 8–13.
- 699 [9] J. N. Ash, R. L. Moses, On optimal anchor node placement in sensor
700 localization by optimization of subspace principal angles, in: *2008 IEEE*
701 *International Conference on Acoustics, Speech and Signal Processing*,
702 IEEE, 2008, pp. 2289–2292.
- 703 [10] B. Tatham, T. Kunz, Anchor node placement for localization in wireless
704 sensor networks, in: *2011 IEEE 7th International Conference on Wire-*
705 *less and Mobile Computing, Networking and Communications (WiMob)*,
706 IEEE, 2011, pp. 180–187.
- 707 [11] S. P. Chepuri, G. Leus, A.-J. van der Veen, Sparsity-exploiting anchor
708 placement for localization in sensor networks, in: *21st European Signal*
709 *Processing Conference (EUSIPCO 2013)*, IEEE, 2013, pp. 1–5.
- 710 [12] H. Sun, O. Büyüköztürk, Optimal sensor placement in structural health
711 monitoring using discrete optimization, *Smart Materials and Structures*
712 24 (12) (2015) 125034.
- 713 [13] K.-V. Yuen, X.-H. Hao, S.-C. Kuok, Robust sensor placement for struc-
714 tural identification, *Structural Control and Health Monitoring* 29 (1)
715 (2022) e2861.
- 716 [14] H. Wang, K. Yao, G. Pottie, D. Estrin, Entropy-based sensor selection
717 heuristic for target localization, in: *Proceedings of the 3rd international*
718 *symposium on Information processing in sensor networks*, 2004, pp. 36–
719 45.

- 720 [15] C. Papadimitriou, J. L. Beck, S.-K. Au, Entropy-based optimal sensor
721 location for structural model updating, *Journal of Vibration and Control*
722 6 (5) (2000) 781–800.
- 723 [16] K.-V. Yuen, S.-C. Kuok, Efficient bayesian sensor placement algorithm
724 for structural identification: a general approach for multi-type sensory
725 systems, *Earthquake Engineering & Structural Dynamics* 44 (5) (2015)
726 757–774.
- 727 [17] S. P. Chepuri, G. Leus, Continuous sensor placement, *IEEE Signal Pro-*
728 *cessing Letters* 22 (5) (2014) 544–548.
- 729 [18] A. Krause, A. Singh, C. Guestrin, Near-optimal sensor placements in
730 gaussian processes: Theory, efficient algorithms and empirical studies,
731 *Journal of Machine Learning Research* 9 (Feb) (2008) 235–284.
- 732 [19] S. Liu, E. Masazade, M. Fardad, P. K. Varshney, Sparsity-aware field
733 estimation via ordinary kriging, in: *2014 IEEE International Conference*
734 *on Acoustics, Speech and Signal Processing (ICASSP)*, IEEE, 2014, pp.
735 3948–3952.
- 736 [20] Y. Chen, J.-A. Francisco, W. Trappe, R. P. Martin, A practical approach
737 to landmark deployment for indoor localization, in: *2006 3rd Annual*
738 *IEEE Communications Society on Sensor and Ad Hoc Communications*
739 *and Networks*, Vol. 1, IEEE, 2006, pp. 365–373.
- 740 [21] J. Liang, M. Liu, X. Kui, A survey of coverage problems in wireless
741 sensor networks, *Sensors & Transducers* 163 (1) (2014) 240.
- 742 [22] R. Zekavat, R. M. Buehrer, *Handbook of position location: Theory,*
743 *practice and advances*, Vol. 27, John Wiley & Sons, 2011.
- 744 [23] D. Fontanelli, F. Shamsfakhr, D. Macii, L. Palopoli, An Uncertainty-
745 driven and Observability-based State Estimator for Nonholonomic
746 Robots, *IEEE Trans. on Instrumentation and Measurement* 70 (2021)
747 1–12, available on line. doi:10.1109/TIM.2021.3053066.
- 748 [24] F. Shamsfakhr, A. Antonucci, L. Palopoli, D. Macii, D. Fontanelli, In-
749 door Localisation Uncertainty Control based on Wireless Ranging for
750 Robots Path Planning, *IEEE Trans. on Instrumentation and Measure-*
751 *ment* 71 (2022) 1–11. doi:10.1109/TIM.2022.3147316.

- 752 [25] D. Fontanelli, F. Shamsfakhr, L. Palopoli, Cramer-Rao Lower Bound
753 Attainment in Range-only Positioning using Geometry: The G-WLS,
754 IEEE Trans. on Instrumentation and Measurement 70 (2021) 1–14.
755 doi:10.1109/TIM.2021.3122521.
- 756 [26] I. Sharp, K. Yu, Y. J. Guo, Gdop analysis for positioning system design,
757 IEEE Transactions on Vehicular Technology 58 (7) (2009) 3371–3382.
758 doi:10.1109/TVT.2009.2017270.
- 759 [27] S. M. Kay, Fundamentals of statistical signal processing, Prentice Hall
760 PTR, 1993.
- 761 [28] C. Wu, W. Su, Y. Ho, A study on gps gdop approximation using support-
762 vector machines, IEEE Transactions on Instrumentation and Measure-
763 ment 60 (1) (2011) 137–145. doi:10.1109/TIM.2010.2049228.
- 764 [29] R. J. Milliken, C. J. Zoller, Principle of operation of navstar and system
765 characteristics, NAVIGATION 25 (2) (1978) 95–106.
- 766 [30] M. P. Fewell, Area of common overlap of three circles, Tech. rep.,
767 DEFENCE SCIENCE AND TECHNOLOGY ORGANISATION ED-
768 INBURGH (AUSTRALIA) MARITIME (2006).
- 769 [31] Y.-C. Wang, C.-C. Hu, Y.-C. Tseng, Efficient placement and dispatch
770 of sensors in a wireless sensor network, IEEE transactions on mobile
771 computing 7 (2) (2007) 262–274.
- 772 [32] J. Zhu, B. Wang, The optimal placement pattern for confident informa-
773 tion coverage in wireless sensor networks, IEEE Transactions on Mobile
774 Computing 15 (4) (2015) 1022–1032.
- 775 [33] R. J. Fowler, M. S. Paterson, S. L. Tanimoto, Optimal packing and
776 covering in the plane are np-complete, Information processing letters
777 12 (3) (1981) 133–137.
- 778 [34] D. S. Hochbaum, Approximation algorithms for the set covering and
779 vertex cover problems, SIAM Journal on computing 11 (3) (1982) 555–
780 556.
- 781 [35] T. H. Cormen, C. E. Leiserson, R. L. Rivest, C. Stein, Introduction to
782 algorithms, MIT press, 2009.

- 783 [36] K. Manohar, B. W. Brunton, J. N. Kutz, S. L. Brunton, Data-driven
784 sparse sensor placement for reconstruction: Demonstrating the benefits
785 of exploiting known patterns, *IEEE Control Systems Magazine* 38 (3)
786 (2018) 63–86.
- 787 [37] Y. Saito, T. Nonomura, K. Yamada, K. Nakai, T. Nagata, K. Asai,
788 Y. Sasaki, D. Tsubakino, Determinant-based fast greedy sensor selection
789 algorithm, *IEEE Access* 9 (2021) 68535–68551.